Crystallization Behavior of αFe in $Fe_{84}Nb_7B_9$ and $Fe_{85}Nb_6B_9$ Amorphous Alloys

Eiichiro Matsubara[1], Satoshi Tanaka[2], Akihiro Makino[3] and Te-Hsuan Chiang[4]

[1]*Institute for Materials Research, Tohoku University, Sendai 980-8577, Japan*
[2]*Dept. Materials Science & Engineering, Tohoku University, Sendai, 980-8579, Japan*
[3]*Dept. Machine Intelligence & System Engineering, Akita Prefectural University, Akita, 015-0055, Japan*
[4]*Institute of Technology Management, Chung Hua University, 30 Tung Shiang Hisn, Chu 30012, Taiwan, R.O. China*

Structures of amorphous $Fe_{84}Nb_7B_9$ (FN7) and $Fe_{85}Nb_6B_9$ (FN6) alloys were investigated by high-energy X-ray diffraction. The structures of FN6 and FN7 contain a relatively large amount of bcc-Fe like clusters. This cluster size seems to grow larger for FN6 than for FN7. From the lattice parameters of αFe precipitates, the crystallization behavior of both alloys were discussed. The αFe precipitates contain supersaturated Nb and B. These solute atoms are removed from αFe by annealing at elevated temperature and stabilize the amorphous matrix. This appears to prevent the growth of αFe to maintain nano-scale αFe particles.

1. Introduction

Fe-based amorphous alloys have been paid a great attention because of their characteristic magnetic properties. The Fe-M-B (M=Zr, Hf, Nb) alloys, composed of about 10-15 nm αFe particles embedded in a small amount of amorphous matrix, show high saturation magnetic induction (Bs) more than 1.5 T as well as good soft magnetic properties.[1,2] Typically, the composition of the M element is 7 at%. The amorphous ribbons are produced by a melt-spinning apparatus placed in a vacuum chamber in order to prevent oxidation of the M elements. This is, however, not desirable from practical view points. Thus, Makino *et al.* tried to reduce Nb content less than 6 at%.[3] They found that since there are already 20-45 nm αFe crystals in the as-quenched $Fe_{85}Nb_6B_9$ alloy, αFe particles show a wide size-distribution in the annealed sample. This deteriorates its soft magnetic property. In the present study, two $Fe_{84}Nb_7B_9$ and $Fe_{85}Nb_6B_9$ amorphous alloys were selected. By substituting 1 at% Nb with 1 at% Fe in $Fe_{84}Nb_7B_9$, a striking difference of crystallization behavior of αFe is observed. Atomic structures of the as-quenched amorphous alloys were investigated by high-energy x-ray diffraction and the details of structures of αFe precipitates were also studied.

We have carried out the studies of local atomic structures and crystallization behavior in Fe-Nb-B amorphous alloys with various B concentrations from 10 to 30 at%.[4–6] In the alloy containing more than 20 at% B, the basic structure of the amorphous phase is a random network structure formed by triangular prisms of 6 Fe(Nb) atoms and 1 B atom,[5] and the metastable $Fe_{23}B_6$ phase is formed before decomposition to the equilibrium phases.[4] By reducing B content to 10 at%, it is known that the atomic structure in the amorphous state cannot be fully explained by the triangular prisms and the metastable phase whose structure is different from $Fe_{23}B_6$ is precipitated.[4] By comparing the present results with the previous ones in the Fe-Nb-B system, we will discuss the structural features of the present alloys.

2. Experimental

The ingots of $Fe_{84}Nb_7B_9$ and $Fe_{85}Nb_6B_9$ alloys were prepared by arc melting the mixtures of pure metals and boron crystal in nominal compositions in an Ar atmosphere. $Fe_{84}Nb_7B_9$ and $Fe_{85}Nb_6B_9$ amorphous ribbons about 20 μm thick and 5 mm wide were prepared by a single-roller melt-spinning technique in an Ar atmosphere. They will be referred to as FN7 and FN6 in the following text, respectively. The densities of FN7 and FN6 determined by Archimedean method are 7.77 and 7.72 Mg/m^3, respectively. Their crystallization behaviors were investigated by the differential scanning calorimeter (DSC) with a heating rate of 0.333 K/s. In order to precisely duplicate the structures observed in the DSC measurements, the as-quenched ribbons were heat-treated in the DSC apparatus with the exactly same conditions.

Diffraction measurements with high-energy x rays of 61.6 keV in the transmission geometry were carried out at BL-04B2 in Spring-8, Harima, Japan. By using high-energy x rays, the spatial resolution in real space is improved due to reduction of truncation errors by extending the upper limit of the wave vector Q_{max} to 250 nm^{-1}. Observed intensities were corrected for background, absorption and polarization.[7] The corrected intensities were converted to absolute units by the generalized Krogh-Moe-Norman method and corrected for the theoretical Compton scattering intensities. A radial distribution function (RDF), $4\pi r^2 \rho(r)$, is obtained by Fourier transformation of the interference function, $Qi(Q)$, calculated from the corrected intensity in absolute units.

$$4\pi r^2(\rho(r) - \rho_0) = rG(r) = \frac{2r}{\pi} \int_0^{Q_{max}} Qi(Q)\sin(Qr)dQ, \quad (1)$$

where $\rho(r) = \sum_{j=1}^N \sum_{k=1}^N x_j f_j f_k \rho_{jk}(r)/\langle f \rangle^2$ and $\langle f \rangle = \sum_{j=1}^N x_j f_j$. The terms ρ, ρ_{jk} and ρ_o are the total number density function, the partial number density function of j-k pairs and the average number density, x_j and f_j are the atomic fraction and atomic scattering factor of the jth element, and N is the total number of constituent elements. A pair distribution function (PDF) is given by $\rho(r)/\rho_o$. Coordination numbers and atomic
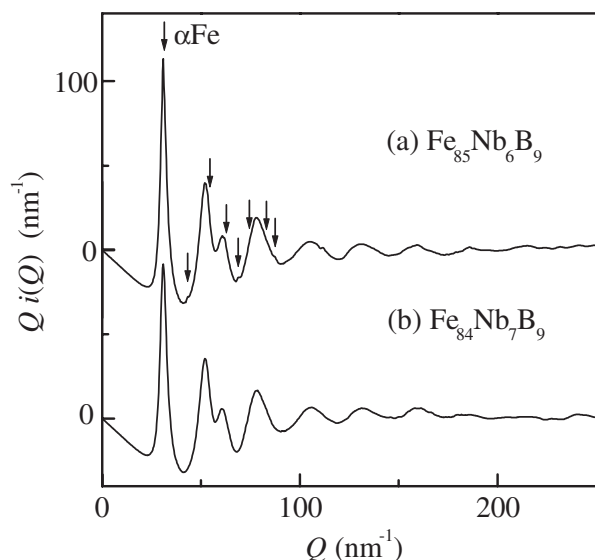
Fig. 1 Interference functions of (a) $Fe_{85}Nb_6B_9$ (FN6) and (b) $Fe_{84}Nb_7B_9$ (FN7) amorphous alloys observed by high-energy x-ray diffraction. Arrows in (a) indicate the peak positions of αFe at low Q-region.

Fig. 2 Pair distribution functions (PDFs) of as-quenched $Fe_{85}Nb_6B_9$ (FN6) and $Fe_{84}Nb_7B_9$ (FN7) alloys are shown by solid and dotted lines, respectively. For comparison, PDF of $Fe_{70}Nb_{10}B_{20}$ amorphous alloy is also shown by a broken line.

distances were determined by fitting the interference function by the non-linear least squares method originally developed by Narten and Levy.[8,9]

X-ray diffraction profiles of the samples annealed in DSC were measured with Ag Kα radiation in the symmetrical reflection geometry. For evaluation of lattice parameters of the precipitated αFe crystals in the annealed samples, diffraction profiles observed with Co Kα were used to improve precision of the extrapolation by Nelson-Riley's method.[10]

3. Results

Interference functions of FN7 and FN6 are shown in Fig. 1. It is clearly seen that good quality diffraction profiles have been obtained even at high-Q in the present measurements. Basic features of the profiles represent an amorphous state, but small peaks of αFe are observed in FN6. Small oscillations of $Qi(Q)$ for FN6 are maintained at larger Q-values. This suggests that a more distinct short-range order (SRO) cluster is grown in FN6. PDFs of both amorphous ribbons computed from the interference functions are shown in Fig. 2. The small peaks of αFe in FN6 were removed from the intensity profile in advance for the calculation of PDF. They are compared with the PDF of the $Fe_{70}Nb_{10}B_{20}$ amorphous alloy in Fig. 2. The atomic structure of the

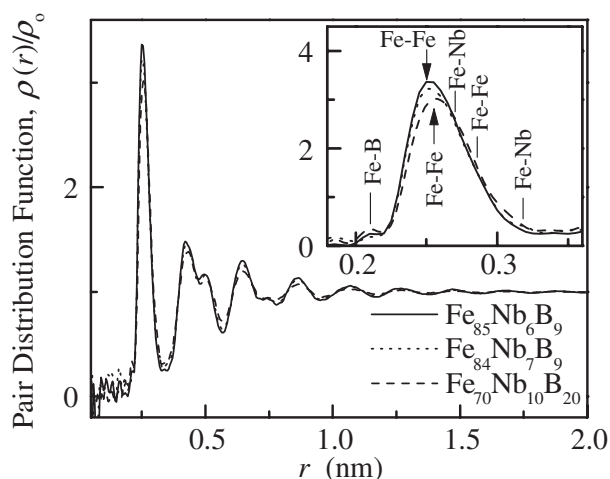$Fe_{70}Nb_{10}B_{20}$ amorphous alloy is a random network structure of the triangular prisms formed by 6 Fe(Nb) atoms at the vertices and 1 B at the center.[5] In order to clearly see the difference among them in local atomic structures at the nearest neighbor distances, the enlarged plot of the first peaks is also shown in Fig. 2. We find that the first peaks of the present alloys are slightly shifted to lower r in comparison with that of the $Fe_{70}Nb_{10}B_{20}$ amorphous alloy. Their peak maximum is located at 0.249 nm instead of 0.254 nm in the $Fe_{70}Nb_{10}B_{20}$ amorphous alloy. The former agrees with the nearest neighbor distance of αFe and the latter corresponds to the first nearest neighbor Fe-Fe pairs of the triangular prism.

In the present analysis, we evaluated coordination numbers and atomic distances by looking for a structural model which gives the best fit to the experimental PDFs by trial and error. In the fitting, the atomic distances calculated from atomic radii of Fe and Nb are used as the initial values of atomic distances of Fe-Fe and Fe-Nb pairs. By assuming a body centered cubic (bcc) Fe like cluster including randomly distributed Nb atoms at Fe sites, we successfully explained the first peaks. Contribution of B in the bcc-like cluster was ignored because it is much smaller than those of Fe-Fe and Fe-Nb pairs. The obtained atomic distances and coordination numbers are summarized in Table 1 with those of αFe for comparison. The atomic distance of Fe-Fe pairs is close to that of αFe and the total coordination number of Fe-Fe and Fe-Nb pairs at the nearest neighbor distances is about 8. This coincides with the values of αFe. In addition, the second

Table 1 Atomic distances and coordination numbers of $Fe_{84}Nb_7B_9$ (FN7) and $Fe_{85}Nb_6B_9$ (FN6) amorphous alloys with those calculated from crystalline data of αFe.

Pairs	$Fe_{84}Nb_7B_9$ (FN7)		$Fe_{85}Nb_6B_9$ (FN6)		αFe	
	r (nm)	N	r (nm)	N	r (nm)	N
B-Fe	0.210 ± 0.002	4.7 ± 1.0	0.210 ± 0.002	3.8 ± 1.0		
Fe-Fe	0.249 ± 0.002	7.1 ± 0.2	0.249 ± 0.002	7.2 ± 0.2	0.248	8.0
Fe-Nb	0.270 ± 0.002	0.9 ± 0.1	0.270 ± 0.002	0.9 ± 0.1		
Fe-Fe	0.285 ± 0.002	3.7 ± 0.2	0.284 ± 0.002	3.7 ± 0.2	0.286	6.0
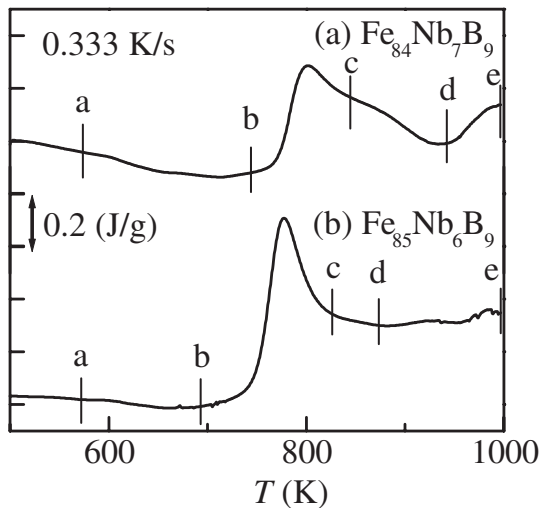
Fig. 3 Differential scanning calorimeter (DSC) profiles of (a) Fe$_{84}$Nb$_7$B$_9$ (FN7) and (b) Fe$_{85}$Nb$_6$B$_9$ (FN6) alloys with a heating speed of 0.333 K/s. Labels are explained in the text.

nearest neighbor Fe-Fe pair is located at the distance close to that of αFe. Consequently, we conclude that the local structure of the present alloys is rather bcc-Fe like clusters than the triangular prism in the alloys containing more than 20 at% B. This is also seen in the fact that coordination number of Fe around B is much less than 6 that is the value when the triangular prism is assumed as the local structural unit.

DSC profiles of FN7 and FN6 are shown in Fig. 3. The as-quenched samples are heat-treated in the DSC apparatus to the temperatures indicated with line segments in Fig. 3, followed by fast quenching to room temperature. Diffraction profiles of these heat-treated FN7 and FN6 alloys are shown in Fig. 4. The FN7 ribbons heat-treated below the onset temperature of the first exothermic peak show no diffraction peaks (a and b) and peaks of αFe appear in the samples heated above the exothermic peak (c, d and e). Thus, it is clearly seen that the first exothermic peak corresponds to the precipitation of αFe.

On the other hand, as mentioned in Fig. 1, the 200 peak of αFe already exists even in the FN6 ribbons heat-treated below the first exothermic peak (a and b). The different appearance of αFe peaks for FN6 in Figs. 1 and 4 is explained by the different geometries used in both measurements. Since the transmission geometry was used in Fig. 1, it provides us the information about crystalline orientation parallel to the ribbon surface. On the other hand, in the symmetrical reflection geometry of Fig. 4, we observe the crystalline orientation normal to the ribbon surface. From these two measurements, we see that the αFe particles of a and b in Fig. 4(b) have a preferred orientation [200] normal to the ribbon surface. These αFe particles clearly grow faster than αFe precipitated by annealing at temperatures above the exothermic reaction. It is also clearly seen that 200 peaks due to Kα$_1$ and Kα$_2$ are separately observed at c to e in Fig. 4(b). These αFe particles correspond to relatively large αFe precipitates in the as-quenched ribbons, observed by transmission electron microscopy by Makino et al.[3] They continue to grow with increase in annealing temperature and are easily
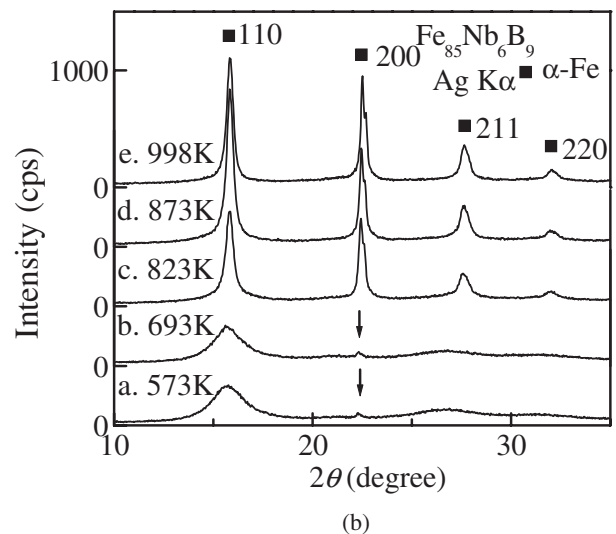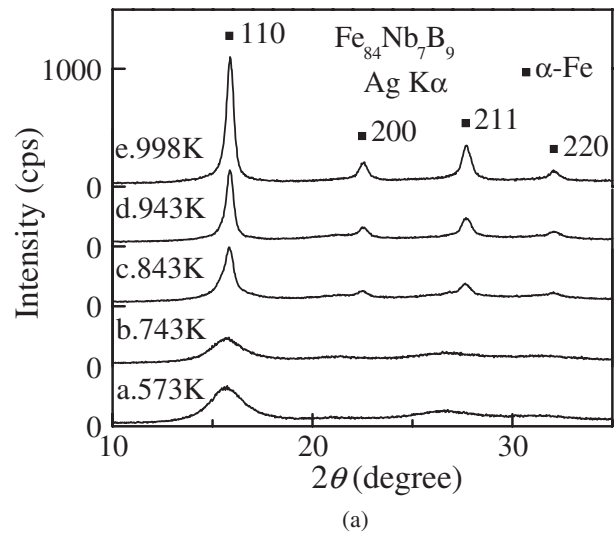

(a)

(b)

Fig. 4 X-ray diffraction profiles of (a) Fe$_{84}$Nb$_7$B$_9$ (FN7) and (b) Fe$_{85}$Nb$_6$B$_9$ (FN6) alloys heat-treated along the DSC curves in Fig. 3 and quenched at the corresponding temperatures (a to e in Fig. 3) in the DSC apparatus.

distinguished from those precipitated above the first exo-thermic peaks (c, d and e), which do not show any clear preferred orientation like that in the as-quenched sample and the peak breadth is much broader because of their smaller crystalline sizes. Consequently, the αFe precipitates with the preferred orientation are heterogeneously nucleated at the ribbon surface and distinguished by those homogeneously nucleated in the amorphous matrix at the elevated temperature.

4. Discussion

The structural analyses of the Fe$_{70}$Nb$_{10}$B$_{20}$ amorphous alloy[5] revealed that the triangular prisms, consisting of a B at the center and 6 Fe atoms at the vertices, are connected by sharing both edges and vertices to form a random network structure.[5] Accordingly, we calculated the number of Fe atoms, which belongs to the triangular prism by selecting different types of combinations of edge- and vertex-sharings so as not to destroy a network of the prisms. Namely, we

Table 2 The number of Fe atoms belongs to the triangular prism in various combinations of edge- and vertex-sharings so as not to destroy a network of the prisms.

The number of Fe atoms per prism	The number of edge-sharings	The number of vertex-sharings
3	2	2
3.5	2	1
4	2	0
4.5	1	1
5	0	2

Fig. 5 Lattice parameters of $Fe_{84}Nb_7B_9$ (■) and $Fe_{85}Nb_6B_9$ (●) evaluated using the peaks of αFe precipitated at the temperatures above the exothermic reactions.

assumed in the calculation that at least two parts of the prism is connected with its neighboring prisms. Furthermore, other types of sharings such as face-sharing are excluded because they are hardly seen in the Fe and B compounds. From the number of Fe atoms in Table 2, we readily evaluated the ratio of Fe to B (R_{FB}) since a B atom is located at the center of the prism. From the table, it is clearly seen that the maximum R_{FB} is 5. Since we know Nb replaces atomic positions of Fe in the Fe-M-B (eq. M=Zr, Nb and Cr) amorphous alloys,[6] it is reasonable that the roles of Nb and Fe in regard to B resemble each other. We find from the present simple calculation in Table 2 that it is hardly keep a network structure in an amorphous $Fe_{80}Nb_{10}B_{10}$ alloy as long as the local unit structure is the triangular prism. The local atomic structure in the $Fe_{80}Nb_{10}B_{10}$ amorphous alloy cannot be really explained only by the triangular prisms.[4] Consequently, it is understandable that bcc like clusters are formed instead of the triangular prisms in the present amorphous alloys, in which the total concentration of Fe and Nb is about 10 times as large as B.

By comparing the diffraction peaks of αFe in Fig. 4, we find that their peak positions are gradually shifted to higher scattering angles with increase in the maximum annealing temperature. In FN7 of Fig. 4(a), the αFe peaks appear above 843 K, that is, above the first exothermic peak of the precipitation of αFe in Fig. 3(a). The similar change of peak positions of αFe is observed in FN6 of Fig. 4(b). Lattice parameters of αFe at each temperature were evaluated from the peaks precipitated above the exothermic reaction. Since αFe with the preferred orientation already exists even below the exothermic peak of FN6, the lattice parameters of αFe for c to e in FN6 were evaluated from the peaks except 200. They are plotted as a function of temperature in Fig. 5. From this figure, a linear relation between the lattice parameter a_o and temperature T was evaluated by the linear least-squares method.

$$a_o \text{ (nm)} = (0.2907 \pm 0.0006)$$
$$- (4.010 \pm 0.616) \times 10^{-6} T \text{ (K)} \quad (2)$$

It is well-known that atoms with a smaller atomic size like B can easily occupy interstitial sites of bcc Fe. Furthermore, Nb has the solid solubility in αFe of 0.095 to 0.330 at% at 873 to 1173 K, respectively.[11] Both lattice parameters of FN6 (0.28669 ± 0.0004 nm) and FN7 (0.28667 ± 0.0004 nm) heated up at 998 K show a value close to pure αFe (0.2866 nm). Therefore, we conclude that the αFe precipitates in the present amorphous alloys contain supersaturated Nb and B. The downside slope in Fig. 5 indicates that these
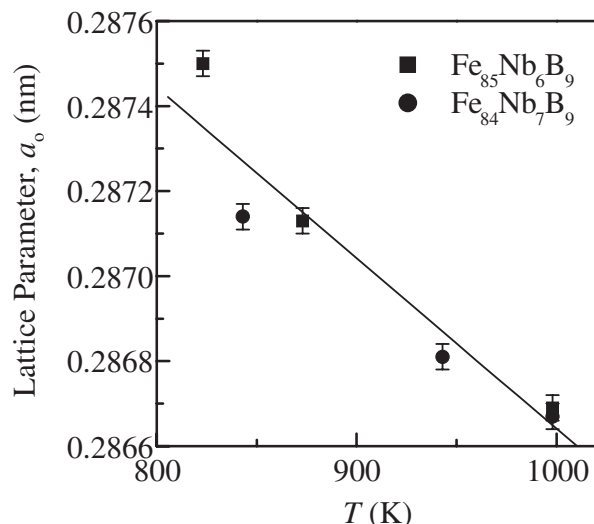
Nb and B atoms are gradually removed from αFe precipitates by heating the samples through a higher temperature. In addition, the peak positions of the 200 peaks with the preferred orientation in Fig. 4(b) also show a gradual shift to higher 2θ. We see that the solute elements are also contained in αFe formed in the as-quenched state and removed with temperature.

With increase in the maximum temperature, Nb and B atoms are removed from the αFe precipitates. Thus, we consider that the concentrations of these elements in the residual amorphous phase increase. From the previous studies of Fe-Nb-B systems, increase in Nb and B contents thermally stabilizes the amorphous state.[12,13] Thus, this will stabilize the Fe-Nb-B amorphous phase and prevent growth of αFe to maintain the nano-scale αFe precipitates.

The difference between the two PDFs is hardly seen in Fig. 2. Only a slight increase in the peak height for Fe-Fe pairs at 0.254 nm is observed. In order to see further details of their difference, the difference between the two reduced RDFs, $G(r)$, in eq. (1), is plotted in Fig. 6. This indicates that the amplitude of $G(r)$ is slightly enhanced in FN6 in comparison with that for FN7 in both short- and medium-range regions. This suggests that the bcc-Fe like region grows larger in FN6. This kind of amorphous structure may deteriorate the thermal stability of the amorphous state to more easily precipitate αFe in the amorphous matrix.

5. Conclusion

In the present study, the atomic structure of the two $Fe_{84}Nb_7B_9$ (FN7) and $Fe_{85}Nb_6B_9$ (FN6) amorphous alloys were investigated by the high-energy X-ray diffraction technique. They show the contrast in the precipitation behavior of αFe that is closely related with a drastic change of the soft magnetic properties. The lattice parameters of αFe were determined from the diffraction peaks in the samples annealed in the DSC apparatus.
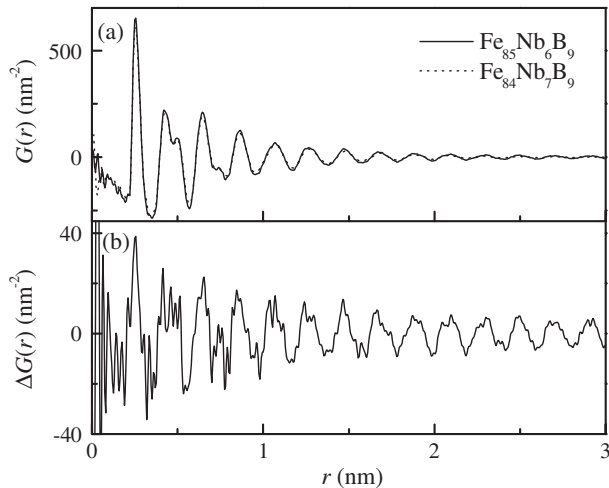
(1) The atomic structures of FN6 and FN7 contain the bcc

Fig. 6 (a) Reduced radial distribution functions, $G(r)$, of Fe$_{84}$Nb$_7$B$_9$ (FN7) (dotted line) and Fe$_{85}$Nb$_6$B$_9$ (FN6) (solid line) amorphous alloys and (b) their difference.

Fe like clusters and are different from those of the amorphous alloys containing more than 20 at% B.

(2) This ordered region extends to a longer distance in FN6.

(3) Nano-scale αFe particles in FN7 and FN6 are homogeneously precipitated by annealing at a temperature above the first exothermic reaction. In FN6, they are distinguished from αFe which appears to be heterogeneously nucleated at the ribbon surface with the [200] preferred orientation.

(4) These αFe precipitates contain supersaturated Nb and B. These Nb and B contents decrease with the maximum annealing temperature and are close to zero above 1000 K.

(5) The solute concentrations of the amorphous matrix increase because Nb and B are removed from αFe precipitates at elevated temperature. This stabilizes the amorphous matrix and appears to prevents the growth of αFe to maintain nano-scale αFe particles.

Acknowledgements

REFERENCES

1) A. Makino, K. Suzuki, A. Inoue, Y. Hirotsu and T. Masumoto: J. Magn. Magn. Mater. **133** (1994) 329–333.
2) A. Makino, A. Inoue and T. Masumoto: Mater. Trans., JIM **36** (1995) 924.
3) A. Makino, T. Bitoh, A. Inoue and T. Masumoto: Scr. Mater. **48** (2003) 869–874.
4) M. Imafuku, S. Sato, H. Koshiba, E. Matsubara and A. Inoue: Mater. Trans., JIM **41** (2000) 1526–1529.
5) E. Matsubara, S. Sato, M. Imafuku, T. Nakamura, H. Koshiba, A. Inoue and Y. Waseda: Mater. Sci. Eng. **A312** (2001) 136–144.
6) T. Nakamura, E. Matsubara, M. Imafuku, H. Koshiba, A. Inoue and Y. Waseda: Mater. Trans. **42** (2001) 1530–1534.
7) Y. Waseda: *The Structure of Non-Crystalline Materials*, (McGraw-Hill, New York, 1980) p. 27–33.
8) A. H. Narten and H. A. Levy: Science **160** (1969) 447–454.
9) E. Matsubara, K. Sugiyama, Y. Waseda, M. Ashizuka and E. Ishida: J. Mater. Sci. Let. **9** (1990) 14–16.
10) H. P. Klug and L. E. Alexander: *X-ray Diffraction Procedures*, 2nd ed. (Wiley-Interscience, New York, 1974) p. 594–597.
11) *Binary Alloy Phase Diagrams*, 2nd ed., ed. by T. B. Massalski, (ASM, Ohio, 1990) p. 1732–1733.
12) A. Inoue and J. S. Gook: Mater. Trans., JIM **36** (1995) 1180–1183.
13) A. Inoue, T. Zhang, T. Itoi and A. Takeuchi: Mater. Trans., JIM **38** (1997) 359–362.